nature synthesis

Article

https://doi.org/10.1038/s44160-024-00494-9

Accelerated discovery of molecular nanojunction photocatalysts for hydrogen evolution by using automated screening and flow synthesis

Received: 26 September 2023

Accepted: 2 February 2024

Published online: 08 March 2024

Check for updates

Weiwei Zhang[1,4], Miaojie Yu[1,2,4], Tao Liu[2], Muyu Cong[1], Xueyan Liu[1], Haofan Yang[2], Yang Bai[2], Qiang Zhu[2], Shuo Zhang[1], Hongxu Gu[1], Xiaofeng Wu[1,2], Zhiyun Zhang[1], Yongzhen Wu[1], He Tian[1], Xiaobo Li[3] ✉, Wei-Hong Zhu[1] ✉ & Andrew I. Cooper[1,2] ✉

Discovering and optimizing multicomponent organic semiconductors is typically a laborious process. High-throughput experimentation can accelerate this, but the results of small-scale screening trials are not always transferable to bulk materials production. Here we report the accelerated discovery of molecular nanojunction photocatalysts based on a combinatorial donor–acceptor molecular library assisted by high-throughput automated screening. The knowledge gained from this high-throughput batch screening is then transferred to a scaled-up, flow-based synthesis process. The scaled-up molecular nanojunction MTPA-CA:CNP147 (3-(4-(bis(4-methoxyphenyl) amino)phenyl)-2-cyanoacrylic acid:2,6-bis(4-cyanophenyl)-4-(4′-fluoro-[1,1′-biphenyl]-4-yl)pyridine-3,5-dicarbonitrile) exhibits a sacrificial hydrogen evolution rate of 330.3 mmol h^{-1} g^{-1} with an external quantum efficiency of 80.3% at 350 nm, which are among the highest reported for an organic photocatalyst. A one-dimensional nanofibre architecture is identified for this molecular nanojunction, which exhibits efficient charge separation. Electronic structure–property correlations across the photocatalyst library show that a moderate binding energy between the donor and the acceptor molecules is a potential factor for efficient molecular nanojunction formation.

Organic semiconductors are important materials for photovoltaics[1–3], displays[4,5], transistors[6,7] and catalysis[8–10]. The traditional approach to designing new organic semiconductors involves iterative optimization of known molecules based on prior knowledge, usually changing one factor at a time. This approach, however, can become laborious as the size of the design space increases. For example, donor–acceptor heterojunction materials offer enhanced performance with respect to single-component materials, but the chemical search space becomes

[1]Key Laboratory for Advanced Materials and Institute of Fine Chemicals, Joint International Research Laboratory of Precision Chemistry and Molecular Engineering, Feringa Nobel Prize Scientist Joint Research Center, Frontiers Science Center for Materiobiology and Dynamic Chemistry, School of Chemistry and Molecular Engineering, East China University of Science and Technology, Shanghai, China. [2]Leverhulme Research Centre for Functional Materials Design, Materials Innovation Factory and Department of Chemistry, University of Liverpool, Liverpool, UK. [3]Key Laboratory of the Ministry of Education for Advanced Catalysis Materials, Zhejiang Key Laboratory for Reactive Chemistry on Solid Surfaces, Institute of Physical Chemistry, Zhejiang Normal University, Jinhua, China. [4]These authors contributed equally: Weiwei Zhang, Miaojie Yu. ✉e-mail: xiaobo.li@zjnu.edu.cn; whzhu@ecust.edu.cn; aicooper@liverpool.ac.uk

https://doi.org/10.1038/s44160-024-00494-9

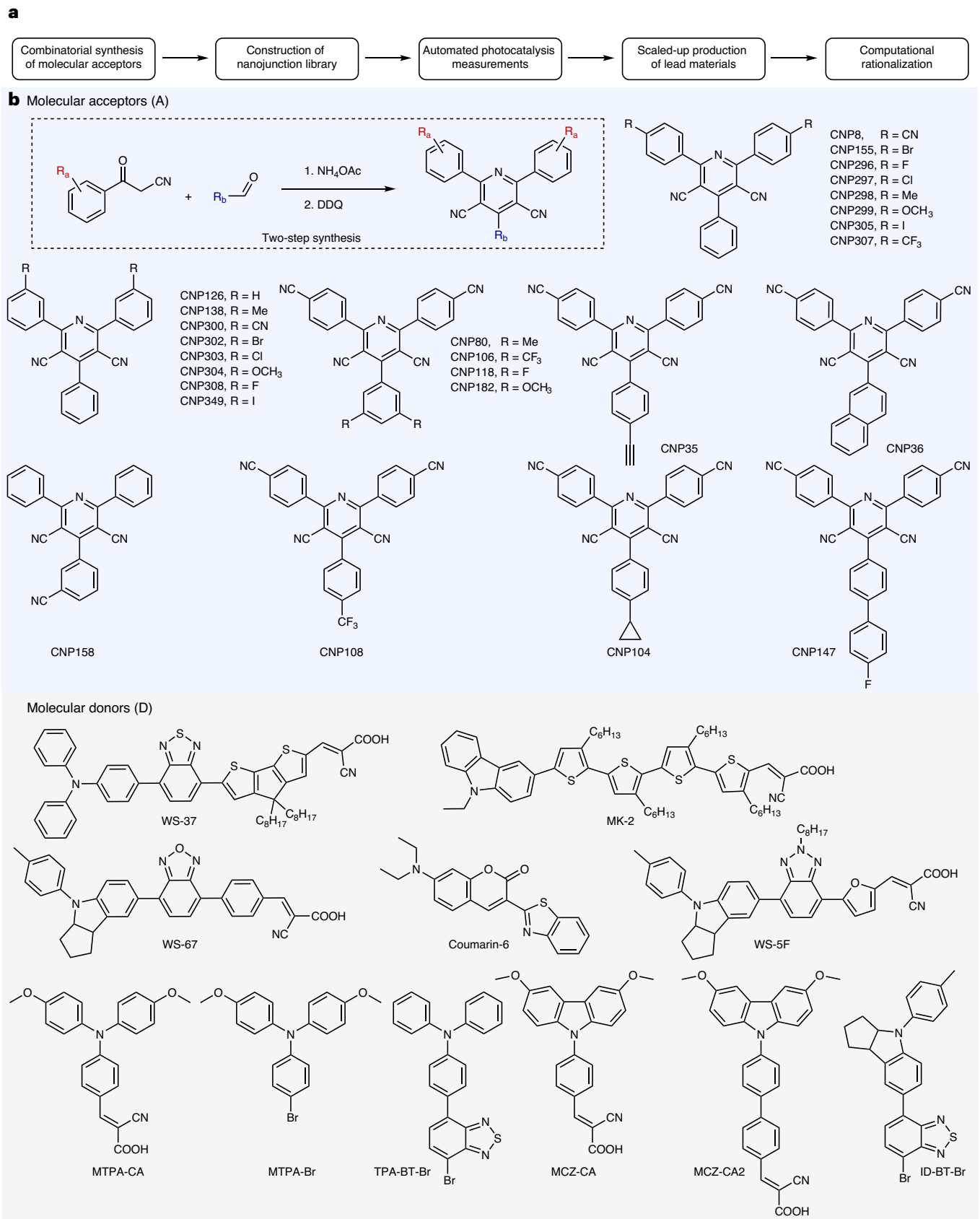

Fig. 1 | Synthesis of combinatorial molecular library. a, Pipeline for accelerated discovery, scale-up and computational rationalization of nanojunction photocatalysts. **b**, Chemical structures of the molecular acceptors (A) and the molecular donors (D). The combinatorial synthesis of CNP acceptors is based on a two-step Hantzsch pyridine synthesis reaction. DDQ, 2,3-dichloro-5,6-dicyano-*p*-benzoquinone.

https://doi.org/10.1038/s44160-024-00494-9

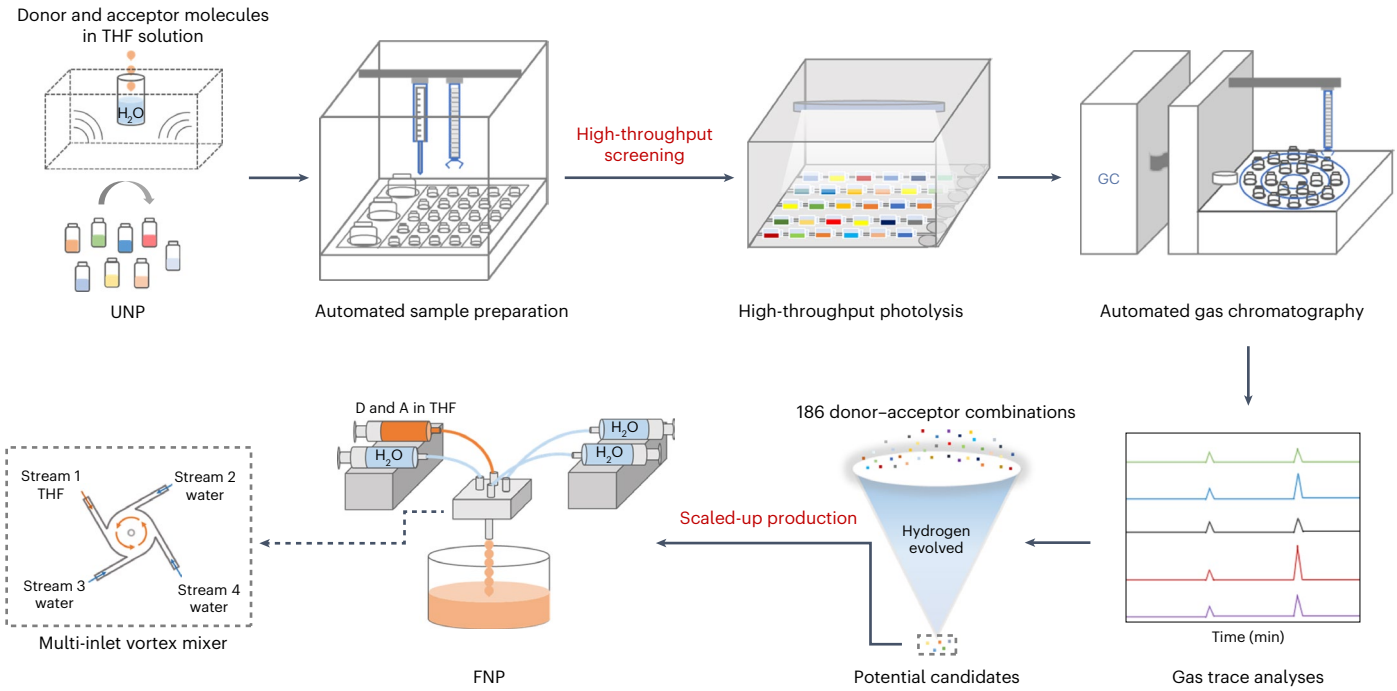

Fig. 2 | Materials acceleration platform for molecular donor–acceptor nanojunction photocatalysts. The acceleration platform for nanophotocatalyst discovery consists of two steps: (1) preparation of a combinatorial molecular nanojunction library by UNP followed by testing for sacrificial hydrogen evolution using an automated photocatalysis workflow; (2) scale-up of the best molecular nanojunctions using an automated FNP processing set-up. A multi-inlet vortex mixer was employed for continuous molecular nanojunction production.

large when one considers the number of organic donors and acceptors that are available. In addition, semiconducting properties are influenced not only by chemical structure but also by the morphology and microstructure of the material, and hence processing conditions are important[11–13]. This can lead to different laboratories reporting quite different properties for what are nominally the same materials. As a result, the development of new organic semiconductors can be a slow process. High-throughput experimentation offers one solution by allowing the simultaneous variation of multiple interrelated factors, and this can be an effective method for identifying new functional materials[14–20]. However, although high-throughput experimentation can expedite materials discovery, it is often limited to small-scale batch screening, and the results are not always transferable to bulk materials production, which presents hurdles for the practical implementation of the screened materials[21–24].

In addition to the established applications mentioned above, organic semiconductor heterojunction nanoparticles have recently gained attention for solar hydrogen production from water[25–30]. Composite nanoparticles that blend a polymer donor and an acceptor molecule can promote exciton dissociation and charge separation, making them promising candidates for photocatalytic hydrogen production. There are also challenges, however, with polymeric semiconductors, such as control over molecular weight, which can affect properties. Small molecules offer some advantages, such as precisely defined chemical structures, ease of purification and, ideally, minimal batch-to-batch variations. This is particularly true if thin films are not required, which has been a major processing advantage for semiconducting polymers. The enhanced crystallization and high phase purity of small molecules can also enable high charge mobility and low energy loss[31]. Small molecules also cover a very broad chemical space, without the necessary criterion of polymerizability. However, until now, small-molecule organic semiconductors have been given relatively little attention as catalysts for photocatalytic hydrogen evolution[32–34].

In this Article we present the accelerated discovery of small-molecule nanojunction photocatalysts by fusing a combinatorial molecular library with an automated screening workflow, followed by 200-fold scale-up using a flow synthesis process (Fig. 1). First, a combinatorial library was synthesized using a Hantzsch pyridine condensation reaction, which generated 26 candidate molecular acceptors (A). These molecular acceptors were combined with a series of candidate molecular donors (D) using ultrasonic nanoprecipitation (UNP) processing (Fig. 2), affording a combinatorial library of 186 donor–acceptor hybrids (156 donor–acceptor pairs in the first-round screening, and a further 30 in the second-round screening; Fig. 3a,b). This library was then tested using a high-throughput photocatalysis screening workflow for sacrificial hydrogen evolution. The most active donor–acceptor materials were scaled-up using a flow-based flash nanoprecipitation (FNP) process. The optimized donor–acceptor molecular nanojunction, MTPA-CA:CNP147 (3-(4-(bis(4-methoxyphenyl)amino)phenyl)-2-cyanoacrylic acid:2,6-bis(4-cyanophenyl)-4-(4′-fluoro-[1,1′-biphenyl]-4-yl)pyridine-3,5-dicarbonitrile) (CNP, cyano-substituted pyridine), showed an exceptionally high sacrificial hydrogen evolution rate (HER) of 330.3 mmol h^{-1} g^{-1} together with an external quantum efficiency of 80.3% at 350 nm. By using this materials acceleration platform, the sample preparation, photocatalytic screening and subsequent scale-up of the best nanophotocatalysts were completed in just tens of days.

Discovering catalysts from a combinatorial molecular library

Combinatorial synthesis in organic chemistry often focuses on metal-based coupling reactions, such as the Suzuki–Miyaura, Stille, Heck and Sonogashira reactions[35,36]. In this work, we synthesized a series of molecular acceptors using a two-step, metal-free Hantzsch pyridine condensation reaction (Fig. 1b and Supplementary Information, section 1). This reaction allowed us to create a library of molecular acceptors that has not been explored previously for photocatalytic hydrogen evolution. Using this method, we substituted the commonly used β-keto ester precursors with β-keto nitriles. The resulting pyridine core thus incorporates two cyano groups (denoted as CNP), imparting the

molecule with an electron-deficient and (predominantly) hydrophilic character[33]. This protocol allows the use of various easily accessible starting materials, thus creating a broad potential chemical search space. We chose a diverse range of molecular functionalities in the library including electron-donating functionalities in the peripheral aryl groups (CNP126, CNP298, CNP138, CNP299, CNP304) and electron-withdrawing groups (CNP308, CNP303, CNP302, CNP349, CNP300). We also varied the substituent position in the peripheral aryl groups (CNP296, CNP297, CNP155, CNP305, CNP8, CNP158, CNP307) and the *para* aryl functionality on the pyridyl ring (CNP106, CNP108, CNP118, CNP104, CNP182, CNP80, CNP35, CNP36, CNP147). The isolated yield for most of these CNP molecules was >50%.

With these electron-deficient CNP acceptor (A) molecules in hand, we next built a molecular nanojunction library by blending them with six different electron-rich molecular donors (D) (WS-37, MK-2, WS-67, Coumarin 6, WS-5F and MTPA-CA). These molecular donors were mostly organic dyes that were developed for dye-sensitized solar cells[37,38]. Even if we only explore a single donor-to-acceptor (D:A) ratio, there are 156 possible binary donor–acceptor combinations (26 acceptors and 6 donors) and 32 single-component systems in this combinatorial library, and it is not obvious, a priori, which combinations to target. This broad chemical space is challenging to explore by sequential manual experiments. To solve this, we paired a UNP method with an automated screening workflow (Fig. 2). The UNP method is easy to operate and demands small quantities of material, making it well suited for high-throughput batch screening, and for other applications beyond photocatalysis. Briefly, the donor and acceptor molecules were dissolved in tetrahydrofuran (THF) solution, and then injected into water under continuous ultrasonication. After evaporation of the THF, colloidal solutions containing donor–acceptor blend nanoparticles were obtained. This molecular library was then tested for sacrificial photocatalytic hydrogen evolution in a high-throughput automated workflow that integrates automated solution preparation (hexachloroplatinic acid and ascorbic acid solution), high-throughput parallel photolysis and automated gas chromatography analysis (Supplementary Information, scheme 2). The parallel photoreactor allowed us to simultaneously test up to 48 samples under uniform illumination conditions with continuous agitation using a roller-plate. This parallel test accelerated the screening and ensured that samples were evaluated under consistent photolysis conditions.

Figure 3a and Supplementary Table 1 summarize the amounts of hydrogen evolved for the binary donor–acceptor pairs in the first-round screen. Most donor–acceptor combinations were inactive under these photocatalysis conditions, but certain combinations—for example, blends of donor MTPA-CA with the acceptors CNP8, CNP35, CNP36 and CNP147—showed high catalytic activities. We therefore performed a second round of screening by blending structural analogues of donor MTPA-CA (MCZ-CA, MCZ-CA2, MTPA-Br, TPA-BT-Br and ID-BT-Br) with a subset of the CNP acceptors. These dyes possess similar donor–acceptor configurations to MTPA-CA, with arylamines as electron donors and cyanoacetic acids or benzothiadiazoles as electron acceptors. In terms of acceptors, our selection was refined to encompass various photocatalytic activity levels, including samples with no activity, moderate activity and high activity. This selection included CNP300, CNP8, CNP35, CNP36, CNP80 and CNP147. While some donor–acceptor combinations with MCZ-CA showed activity, nanojunctions with MTPA-CA outperformed those formed with its six structural analogues (Fig. 3b and Supplementary Table 2). Overall, the five donor–acceptor combinations that were the most effective molecular nanojunction photocatalysts under these conditions were MTPA-CA:CNP8, MTPA-CA:CNP35, MTPA-CA:CNP36, MCZ-CA:CNP36 and MTPA-CA:CNP147. These results show how sensitive the photocatalytic activity is to small structural changes; for example, there are four structurally analogous fluorinated acceptors, CNP106, CNP108, CNP118 and CNP147, but CNP147 leads to by far the most active donor–acceptor nanojunction (Supplementary Fig. 32).

The automated screening workflow allowed us to identify active donor–acceptor nanojunctions from a total of 186 donor–acceptor combinations in just 3 days, excluding the time required for the molecular synthesis of the donors and acceptors. While the synthesis of the molecular building blocks was not automated, and remains a time-consuming step, our method represents a large time saving because even a modest number of donors and acceptors can lead to a huge compositional space, particularly when dealing with ternary nanohybrid materials. Hence, fusing the high-throughput automated screening and combinatorial molecular library markedly accelerates the material discovery process compared to conventional, manual methods, and this benefit would scale even more if we consider more complex structures in the future, such as quaternary nanohybrids.

From high-throughput screening to scale-up flow synthesis

It is well known in drug discovery that high-throughput screening on a small scale can lead to 'hits' that are subsequently not scalable to bulk syntheses. Likewise, small-scale nanoprecipitation methods involve ultrasonication that is challenging on a larger scale, and the resulting nanophotocatalysts may not be representative of scaled-up materials. We therefore used a flow-based FNP method for scale-up[39] and compared the activities of these scaled-up materials with the screening samples. FNP uses a multi-inlet vortex mixer system to rapidly mix an organic solvent (here THF) with an antisolvent (here water). Due to the flow-based continuous operation, this method can be used to prepare nanoparticulate materials in large quantities. Here, the mass production capability of FNP serves as an ideal complement to UNP that is more suitable for the rapid synthesis of materials at the screening scale. The molecular nanojunctions that showed high activities in small-scale screening experiments all exhibited high photocatalytic HERs when processed by FNP, with the highest rate being 214.4 mmol h^{-1} g^{-1} for MTPA-CA:CNP147 (Fig. 3c,d). As a control, MTPA-CA:CNP126, which was inactive in the initial screening experiments, still showed low activity when scaled-up using FNP. This shows that the insights gained from high-throughput screening can be applied to scaled-up production.

We next sought to develop a more optimized molecular nanojunction photocatalyst based on the best-performing donor–acceptor combination (MTPA-CA:CNP147) using FNP processing. As shown in Fig. 3e, the molecular ratio of the donor and acceptor was optimized to regulate interfacial exciton dissociation. Increasing the mass fraction of the CNP147 acceptor increased the average HER up to a maximum of 259.8 mmol h^{-1} g^{-1} at around 4:6 wt/wt MTPA-CA:CNP147. A further increase in the CNP147 mass fraction gave lower activities. The particle size distributions of the donor–acceptor nanojunctions were only slightly affected by the donor–acceptor blend ratio, despite the large variation of HER (Supplementary Fig. 14), suggesting that this is not a particle size effect. Optimizing the platinum loading enhanced the HER further, and a maximum activity was obtained at 9 wt% platinum (Supplementary Fig. 16). This optimized molecular nanojunction (MTPA-CA:CNP147, 4:6 wt/wt, 9 wt% Pt) produced 2,576 µmol hydrogen over 5 h photolysis using 1.56 mg catalyst, corresponding to an exceptional mass-normalized HER of 330.3 mmol h^{-1} g^{-1} (full spectrum, average light intensity, 289 mW cm^{-2}, Fig. 3f). This HER outperforms most other reported organic photocatalysts (Supplementary Table 18). A high activity of 157.5 mmol h^{-1} g^{-1} was also achieved under AM 1.5G irradiation. We also measured the catalytic activity for a physical mixture of individual nanoparticles (MTPA-CA and CNP147), which displayed a much lower HER of 66.6 mmol h^{-1} g^{-1}, showing that nanojunction construction is required for these high activities.

The external quantum efficiency (EQE) of the best molecular nanojunction (MTPA-CA:CNP147, 4:6 wt/wt) was measured at different wavelengths (Fig. 3g). A maximum EQE of 80.3% was obtained at 350 nm (72.5% at 365 nm; 19.9% at 400 nm; 8.5% at 420 nm; 3.7% at 500 nm). We note that the highest EQE was achieved at the absorption overlap of

https://doi.org/10.1038/s44160-024-00494-9

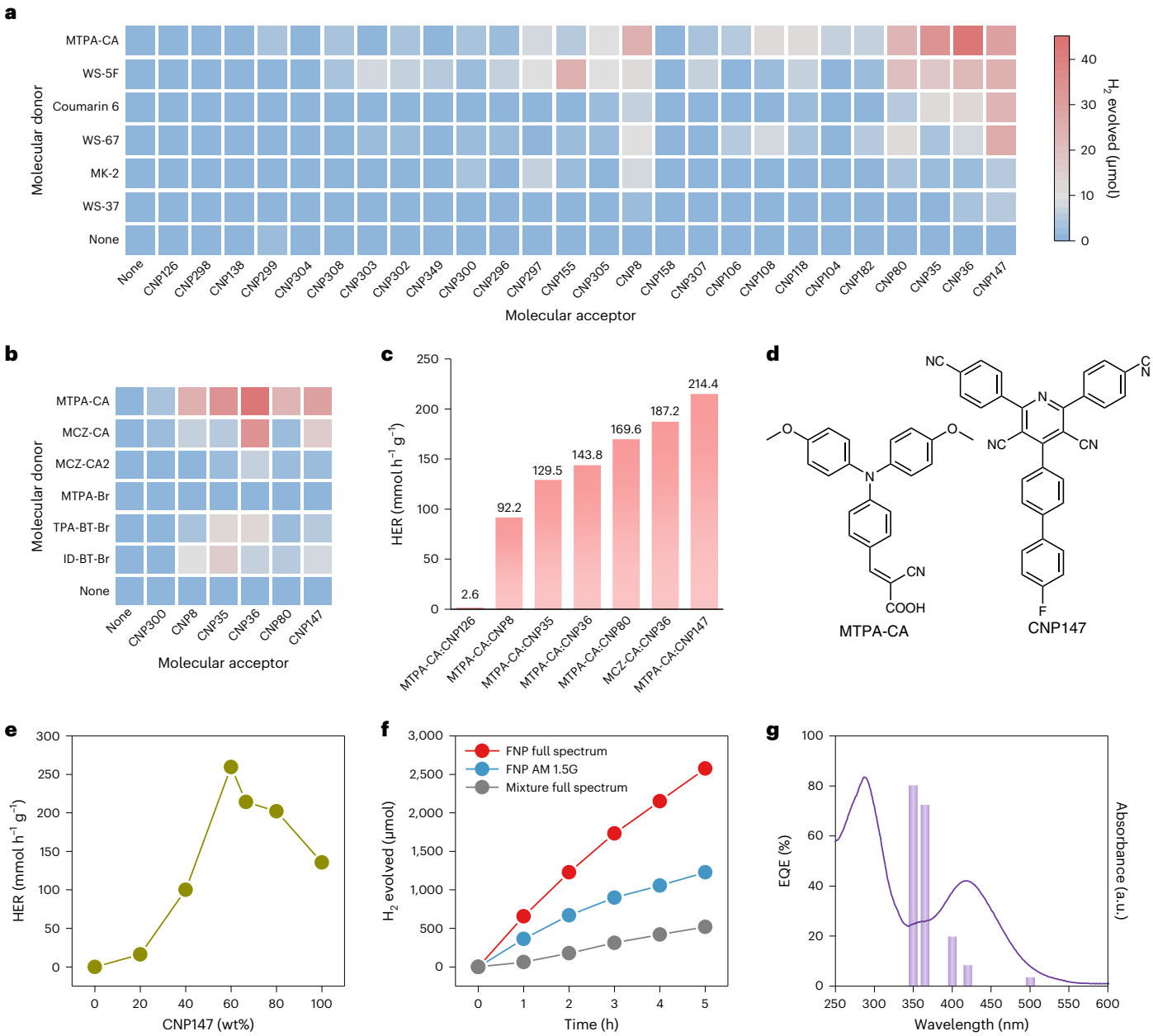

Fig. 3 | Photocatalytic activities of molecular nanojunctions prepared by UNP and scaled-up using FNP. a,**b**, Plots showing amount of hydrogen produced for 186 donor–acceptor molecular nanojunction photocatalysts prepared by UNP in the first screening round (**a**) and a second screening round (**b**) under AM 1.5G irradiation (average light intensity, 100 mW cm^{-2}). **c**, HERs of identified donor–acceptor combinations (MTPA-CA:CNP8, MTPA-CA:CNP35, MTPA-CA:CNP36, MTPA-CA:CNP80, MCZ-CA:CNP36 and MTPA-CA:CNP147) that were scaled-up using FNP. Note that MTPA-CA:CNP126 was inactive in high-throughput screening and was included in the FNP scale-up as a control. **d**, Chemical structures of the components of the best-performing donor–acceptor combination, MTPA-CA (D) and CNP147 (A). **e**, Average HERs of MTPA-CA:CNP147 blend nanojunction photocatalysts formed by FNP using different donor–acceptor mass ratios; around 60 wt% CNP147 is optimal. Photocatalysis conditions: 1.56 mg photocatalyst, 25 ml H_2O, 3 wt% platinum based on molecular nanojunction as a co-catalyst, 0.2 M ascorbic acid. **f**, Time courses for photocatalytic hydrogen evolution of MTPA-CA:CNP147 (4:6 wt/wt) formed by FNP under optimal catalytic conditions irradiated by a xenon lamp with full spectrum and AM 1.5G, respectively (average light intensities, 289 and 100 mW cm^{-2}, respectively), and a comparison with a simple physical mixture of the respective nanoparticles of the individual components, MTPA-CA and CNP147. **g**, EQEs of MTPA-CA:CNP147 (4:6 wt/wt) nanophotocatalysts formed by FNP measured at 350, 365, 400, 420 and 500 nm, overlaid with the ultraviolet–visible absorption spectrum for the donor–acceptor nanojunction.

the intramolecular charge transfer (ICT) band of individual MTPA-CA and CNP147 nanoparticles (Supplementary Fig. 13b), indicating the synergetic effect of donor–acceptor molecules on their photocatalytic performances; that is, simultaneous excitation of both components[25]. Given the electron-donating nature of the electron-rich, methoxy-substituted MTPA-CA triphenylamine, and the electron-withdrawing nature of the electron-deficient cyano-decorated CNP147 pyridine, we believe that the two components operate as a type II heterojunction. In this case, electron transfer from MTPA-CA excitons to CNP147, and hole transfer from CNP147 excitons to MTPA-CA, would occur[13], as supported by a change in the steady-state fluorescence spectrum, discussed below. This EQE is also among the highest reported for organic photocatalysts for sacrificial hydrogen production (Supplementary Table 18). We further verified the scalability of the molecular

https://doi.org/10.1038/s44160-024-00494-9

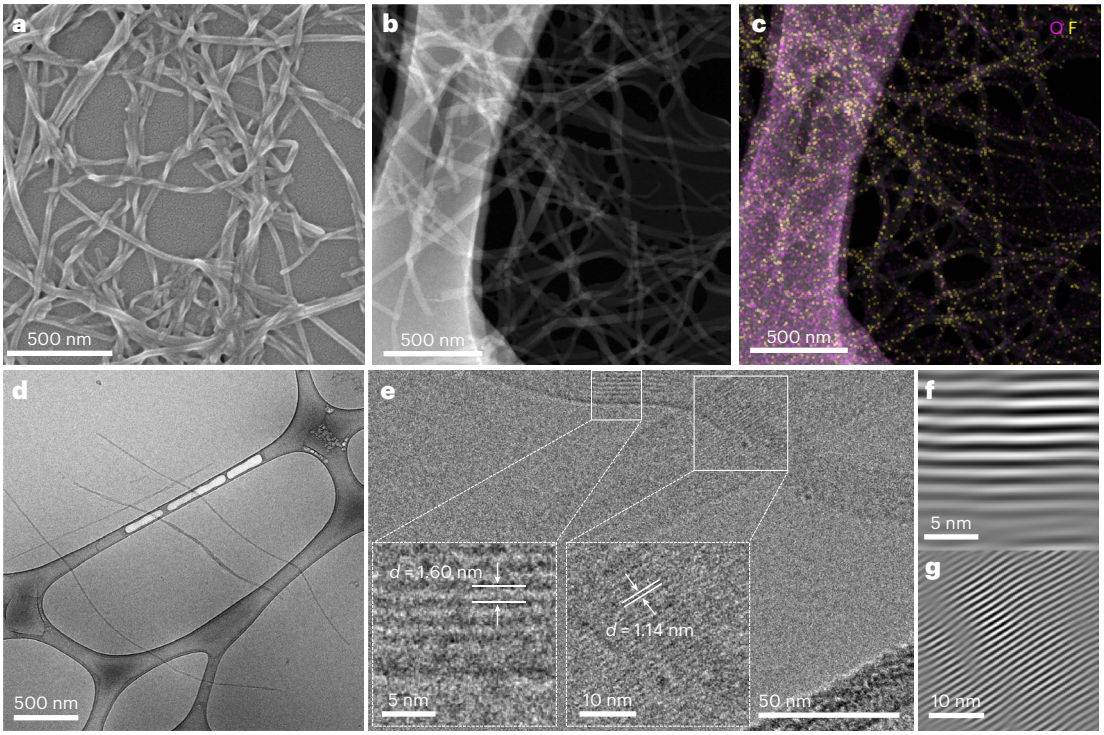

Fig. 4 | Morphology and crystallinity of MTPA-CA:CNP147 molecular nanojunctions. a–**c**, SEM image (**a**), high-angle annular dark-field scanning transmission electron microscopy image (**b**) and EDX mapping analysis of oxygen (purplish red) and fluorine (yellow) (**c**) of the MTPA-CA:CNP147 (4:6 wt/wt) molecular nanojunction formed by FNP. **d**, Cryo-TEM image of MTPA-CA:CNP147 nanojunction photocatalyst showing the fibre morphology. **e**, High-resolution cryo-TEM image of MTPA-CA:CNP147 nanofibres. Insets: crystalline domains in these nanofibres taken from the regions highlighted by the white squares. **f**,**g**, Filtered inverse fast Fourier transform images corresponding to the insets in **e**.

nanojunction production by FNP by increasing the stock solution to produce more than 1 litre of catalytic solution; in principle, this amount could be increased to any scale because of the continuous operation of FNP. This scaled-up 1 litre solution (200-fold with respect to the high-throughput test; Supplementary Fig. 22) gave a comparable HER of 305.4 mmol h^{-1} g^{-1}. Scanning electron microscopy (SEM) images suggested nearly identical morphologies for the scaled-up photocatalysts and the materials produced for screening (Supplementary Fig. 24).

Efficient charge separation in molecular nanojunction fibres

The morphology of the optimized MTPA-CA:CNP147 molecular nanojunctions prepared by FNP processing was imaged by SEM, scanning transmission electron microscopy and energy-dispersive X-ray (EDX) mapping. These revealed a one-dimensional nanofibre architecture with a width of ~30 nm and a length of several micrometres (Fig. 4a,b). EDX mapping showed that oxygen-containing MTPA-CA and fluorine-containing CNP147 overlapped on a single nanofibre (Fig. 4c); that is, there was no evidence for phase segregation at this resolution. Cryo-transmission electron microscopy (cryo-TEM) can image catalysts in a near-natural state, which further confirmed the nanofibre morphology, and the length of these fibres was 2 µm or longer (Fig. 4d). At higher resolutions (Fig. 4e–g), crystalline domains were observed and the lattice spacings were 1.60 and 1.14 nm, respectively, indicating the crystalline nature of these nanofibres. As acquired from cryo-TEM, these lattice spacings matched with the powder X-ray diffraction (PXRD) diffraction peaks of the freeze-dried MTPA-CA:CNP147 nanofibres (Fig. 5a, $2\theta = 5.5$ and 8.5°). Both the sample morphology and the PXRD patterns of the MTPA-CA:CNP147 molecular nanojunctions resembled those of catalysts formed using a single-acceptor component, CNP147. No diffraction peak for the MTPA-CA component was found in the heterojunction sample, even though that component was present at 40 wt%. We therefore speculate that the MTPA-CA component might be deposited onto the CNP147 nanofibres as an amorphous coating.

Many polymer–polymer and polymer–small-molecule blend nanophotocatalysts have spherical morphologies with diameter of tens of nanometres[13,27]. The intimately mixed donor–acceptor components in such nanospheres afford large interfacial areas for exciton dissociation, but also increase the possibility of charge recombination, limiting the free charges that can be utilized for photocatalytic reactions. A recent study indicated that such charge carrier recombination can be alleviated by increasing the mass ratio of acceptors in the donor–acceptor heterojunction with improved crystallinity and better phase segregation[40]. In contrast to these polymer-based nanophotocatalysts, our molecular nanojunctions were nanofibres with a length of a few micrometres. The molecular nanofibres are substantially crystalline, at least in terms of the CNP147 component. Both this morphology and the composition of the molecular nanojunctions are considered to be favourable for the high photocatalytic activity that is observed[40,41].

The energy-level alignments for MTPA-CA and CNP147 were estimated from their absorption spectra and cyclic voltammograms, which indicated a type II energy-level offset (Fig. 5b). The large overpotential between the lowest unoccupied molecular orbital (LUMO) levels of MTPA-CA and CNP147 and the proton reduction level creates a driving force for efficient photocatalytic hydrogen evolution reaction. However, as shown in Supplementary Fig. 9, these energy levels alone cannot rationalize the uniquely high activity of the MTPA-CA:CNP147 combination: many other donor–acceptor pairs have similar overpotentials but show low catalytic activity. Figure 5c shows the ultraviolet–visible absorption spectra of individual MTPA-CA, CNP147 and MTPA-CA:CNP147 (4:6 wt/wt) blend nanoparticle dispersions formed by FNP. CNP147 primarily absorbs ultraviolet light and has an ICT absorption peak located at 355 nm, while MTPA-CA has strong

https://doi.org/10.1038/s44160-024-00494-9

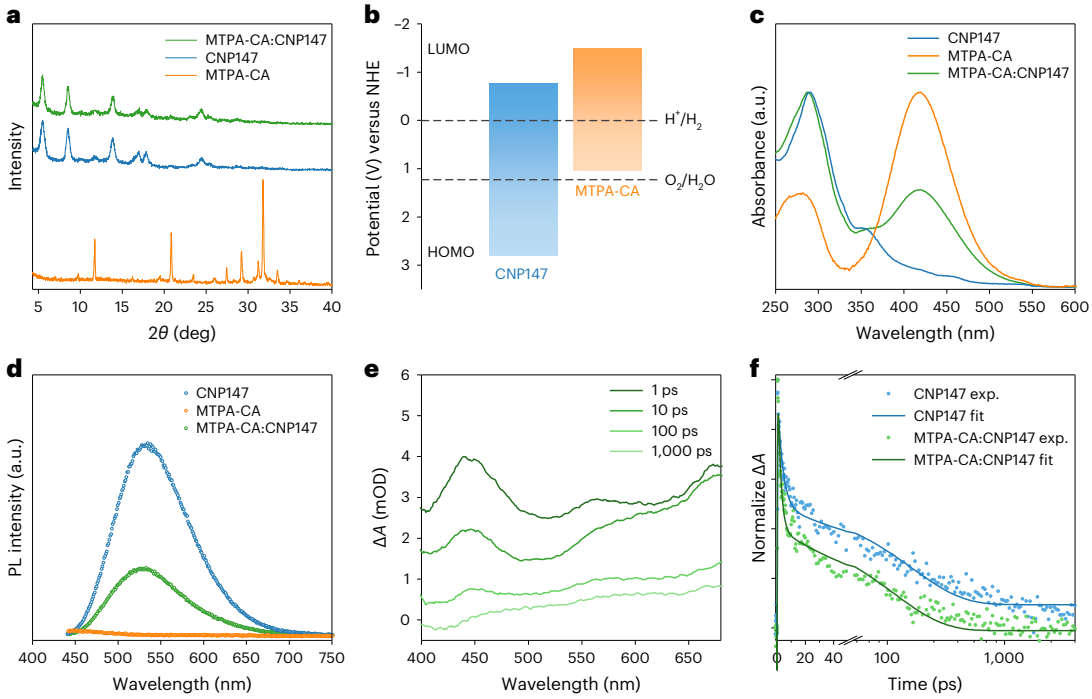

Fig. 5 | PXRD and photophysical properties of MTPA-CA:CNP147 molecular nanojunction photocatalyst. a, PXRD patterns of freeze-dried MTPA-CA:CNP147 nanofibres, and comparison with individual CNP147 and MTPA-CA processed by FNP. **b**, Energy-level diagrams of CNP147 and MTPA-CA. **c**,**d**, Ultraviolet–visible absorption (**c**) and photoluminescence (**d**, excited at 290 nm) spectra of MTPA-CA and CNP147 nanoparticles, and MTPA-CA:CNP147 (4:6 wt/wt) nanojunction in water dispersion. **e**, Transient absorption spectra of MTPA-CA:CNP147 (4:6 wt/wt) nanojunction at different time delays pumped at 320 nm (ΔA (mOD), change in absorbance, where the mOD is the milli-optical density). **f**, Comparison of transient absorption decay dynamics for CNP147 and MTPA-CA:CNP147 processed by FNP pumped at 320 nm and probed at 450 nm.

absorption band in the visible light range with a peak absorption at 418 nm. MTPA-CA:CNP147 (4:6 wt/wt) blend nanoparticles exhibit the absorption characteristics of both MTPA-CA and CNP147, absorbing light across the spectrum from the ultraviolet to the visible range.

Photoluminescence (PL) spectra were recorded to explore the exciton dissociation in the MTPA-CA:CNP147 molecular nanojunction formed by FNP (Fig. 5d). MTPA-CA nanoparticles showed very low PL intensities in water dispersion, whereas CNP147 nanoparticles displayed an intense emission at around 530 nm (when excited at 290 nm). A distinct photoluminescence quenching was found for MTPA-CA:CNP147 nanojunctions compared with CNP147 nanoparticles, indicative of efficient exciton dissociation. This quenching was more pronounced when the content of MTPA-CA in the molecular nanojunction was increased (Supplementary Fig. 13f). Compared with single-component CNP147 nanoparticles, a shortened emission lifetime was also observed for the binary nanojunctions, providing further evidence for charge transfer in the MTPA-CA:CNP147 hybrids (Supplementary Fig. 33). The charge separation was also illustrated by ultrafast transient absorption spectroscopy (Fig. 5e,f). Upon excitation of single-component CNP147 at 320 nm, a broad photoinduced absorption band from 400 to 680 nm emerged that overlapped with its PL band. This excited-state absorption located at 450 nm was found to decay faster when blending with MTPA-CA. The phenomenon aligns with the change observed in steady-state PL and emission lifetime, which could result from excited-state charge transfer from CNP147 to MTPA-CA. However, the electron transfer from MTPA-CA to CNP147 was hard to determine from transient absorption spectroscopy because of the very different morphologies for single-component MTPA-CA and the MTPA-CA:CNP147 nanojunctions. MTPA-CA by itself can only form large non-fluorescent aggregates in aqueous solutions due to its hydrophobicity, and hence bulk charge transfer might dominate (Supplementary Fig. 36). The electron transfer from MTPA-CA to CNP147 in the nanojunction was investigated by measuring the PL change in the nanojunction compared with individual MTPC-CA under 450 nm excitation (Supplementary Fig. 13d), along with photocatalysis tests under irradiation beyond 420 nm (Fig. 3g and Supplementary Fig. 20). These results indicate the possible electron transfer from MTPA-CA to CNP147 under visible light irradiation.

Donor–acceptor binding energy as a potential descriptor

With photocatalysis data in hand for 186 donor–acceptor combinations, we proceeded to investigate the underlying factors that dictate photocatalytic activity variation in molecular nanojunctions using theoretical calculations (Supplementary Fig. 30). To begin with, we conducted sampling of suitable geometric points surrounding each donor and systematically tested each acceptor on these sampled points to construct initial candidate donor–accpetor pair structures. We then employed the recently developed geometry, frequency, non-covalent, extended tight binding (GFN-xTB) method, implemented in xTB[42,43], to optimize these pairs and obtain preferred geometries that express the highest binding energy for all donor–acceptor combinations. Finally, these stable donor–acceptor interface structures were reoptimized at the DFT/CAM-B3LYP[44]/Def2-svp[45,46] level by Gaussian16 (ref. 47). Binding energy (E_b) was calculated from the equation $E_b = |E_{D:A} - E_D - E_A|$, where $E_{D:A}$ represents the energy of the donor–acceptor interface, and $E_{D(A)}$ represents the energy of the isolated D(A) molecules. To gain insight into the other relevant factors affecting the HER, electronic couplings, V_{L-L} and V_{H-L}, were obtained by calculating the charge transfer integral between different orbitals[48]. V_{L-L} represents the electronic coupling between the LUMOs of the donor and acceptor molecules, and V_{H-L} represents the electronic coupling between the highest occupied molecular orbital (HOMO) of the donor and the LUMO of the acceptor. V_{L-L} is usually correlated with interfacial charge separation, which is beneficial for HER, while V_{H-L} is related to charge recombination, which is one of the primary loss mechanisms both in photocatalytic

https://doi.org/10.1038/s44160-024-00494-9

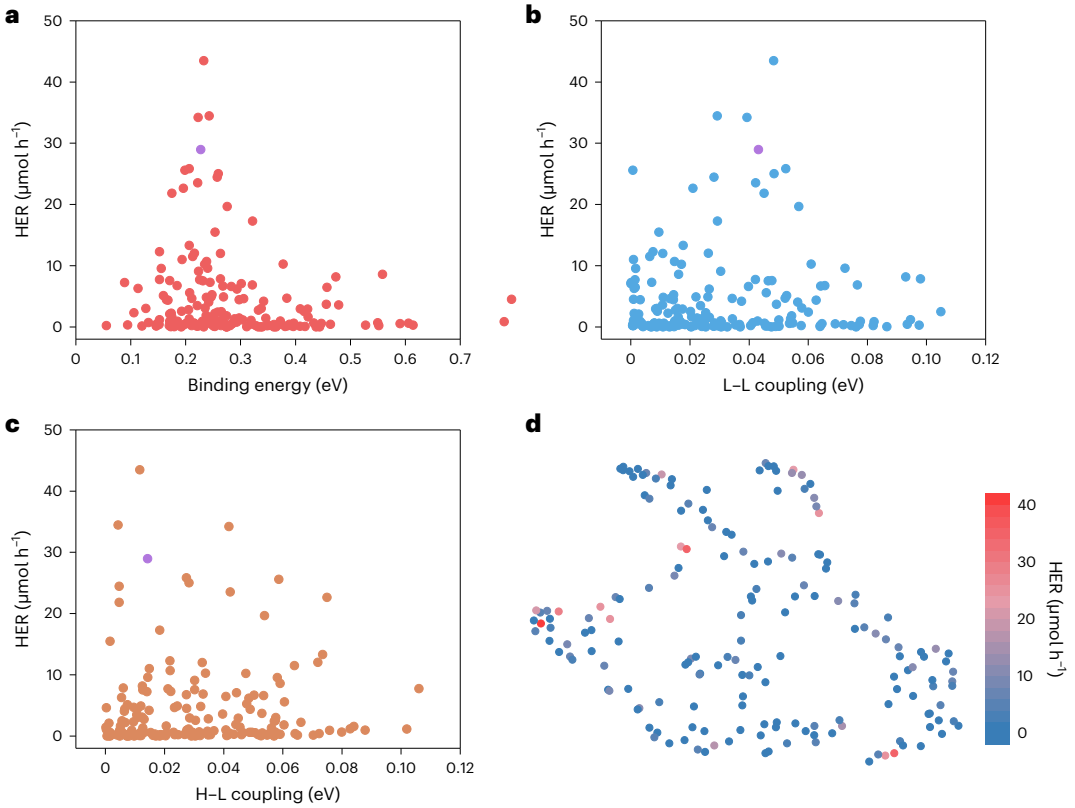

Fig. 6 | Density functional theory calculations for molecular nanojunction photocatalysts. a, The HER as a function of binding energy, E_b, of the donor and acceptor dimer pairs (MTPA-CA:CNP147 highlighted in purple). **b**,**c**, The HER as a function of the coupling between the LUMO of the donor and the LUMO of the acceptor, V_{L-L} (**b**), and between the HOMO of the donor and the LUMO of the acceptor, V_{H-L} (**c**) (MTPA-CA:CNP147 highlighted in purple). **d**, Two-dimensional UMAP embeddings of the V_{L-L}–V_{H-L}–E_b relationship space, colour coded by the HER.

water splitting and in other photoinduced applications involving hot electrons and holes, such as photovoltaics[49].

Intriguingly, we found a volcano-like trend where the best HER values of donor–acceptor pairs are located within binding-energy range of 0.15–0.25 eV (Fig. 6a). Deviations from this range to either stronger or weaker binding energies resulted in lower photocatalytic activities. Likewise, HER also exhibits a volcano-like pattern against V_{L-L} (Fig. 6b), with the best HER falling within the range of 0.02–0.06 eV. In contrast, there is a monotonic decrease in HER as a function of V_{H-L} (Fig. 6c). In all cases, it appears that an optimal binding energy and electronic coupling are necessary for an efficient donor–acceptor combination. We note that the volcano-like trend was particularly pronounced for HER and E_b, suggesting that binding energy could be a potential factor affecting the activity of organic heterojunction photocatalysts, similar in importance to parameters such as redox driving forces and light absorption. To visualize the relationship between V_{L-L}, V_{H-L} and E_b, we plotted Fig. 6d assisted by the Uniform Manifold Approximation and Projection (UMAP) dimension-reduction method[50], colour coded by the HER. This technique reduces data from a high-dimensional space to a two-dimensional space suitable for plotting, while aiming to preserve the local distance and global structure present in the original space. The plot reveals a subtle tendency for high-HER combinations to cluster together. Moreover, points in close proximity on this plot, which have similar V_{L-L}, V_{H-L} and E_b values, often share the same donor or acceptor, although no universally applicable pattern was identified. We acknowledge that other factors are important that are not captured in these calculations, such as particle morphology and surface hydrophilicity (Supplementary Table 4); this can explain the presence of inactive photocatalysts with similar binding energy or descriptor values to the active donor–acceptor combinations. Photocatalysis is a process influenced by multiple factors, and an appropriate binding energy can be a necessary but not sufficient condition. We note also that the optimized calculated donor–acceptor pair geometries might not always be expressed in the nanojunctions, and as such, these calculations serve as a guide only.

Conclusions

We have established a materials acceleration platform for the discovery of molecular nanojunction photocatalysts by combining combinatorial molecular libraries, high-throughput automated catalyst screening and scaled-up flow synthesis. By leveraging the advantages of two nanomaterial synthesis methods, UNP and FNP, we have effectively bridged the gap between small-scale, high-throughput screening and large-scale production. The optimal molecular nanojunction, MTPA-CA:CNP147, exhibited an exceptional sacrificial HER up to 330.3 mmol h^{-1} g^{-1} with an EQE of 80.3% at 350 nm, and this nanophotocatalyst could be produced on at least the 1 litre scale by flow synthesis. These nanojunctions had a one-dimensional nanofibre morphology, and photophysical characterization showed efficient charge separation. Analysis of the correlation between electronic structure and photocatalytic activity for this library of 186 photocatalysts revealed that a moderate binding energy between the molecular donor and the acceptor led to the highest photocatalytic activities, thereby providing a design rule for other organic heterojunction photocatalysts in the future. Although we have focused here on sacrificial photocatalytic hydrogen production, the same combined experimental and computational platform could accelerate the discovery of molecular heterojunction nanomaterials for other applications that require available photogenerated electrons and holes, such as photo-organocatalysis and photovoltaics. Moreover, the same general principle of coupling small-scale screening with scaled-up

flow synthesis might be used to discover totally different materials, such as organic nanoparticles for drug delivery, again exploiting the transferability of screening to scale-up.

Methods

General synthesis procedures for CNP molecules

The CNP molecules were synthesized using the Hantszch pyridine condensation reaction with modifications (Fig. 1b). In general, a reaction flask was charged with R_a (3.0 mmol), R_b (1.5 mmol) and ammonium acetate (7.5 mmol), and then glacial acetic acid (15.0 ml) was added. The reaction mixture was heated to 110 °C overnight. The resulting precipitates were filtered and washed with methanol. Then, the solids were oxidized with 2,3-dichloro-5,6-dicyano-*p*-benzoquinone in acetic acid solution at 110 °C for 1 h, followed by filtration and washing with methanol. The solids were purified by column chromatography using hexane/ethyl acetate as eluent, giving the final product as a white or light-yellow solid (the total isolated yield was >50% for most CNP molecules).

UNP for high-throughput screening

For UNP, donor molecules and acceptor molecules were dissolved in THF at concentrations of 0.5 mg ml^{-1} and 1.0 mg ml^{-1}, respectively, as stock solution. These stock solutions of donor (0.30 ml) and acceptor (0.30 ml) were mixed with a surfactant, S1 (0.12 ml, 1.0 mg ml^{-1} in THF, see chemical structure in Supplementary Fig. 2), and ultrasonicated for 5 min. The resulting solution mixture (0.50 ml) was added rapidly into a vial containing deionized water (5.0 ml) under continuous ultrasonication for 10 s. The resulting vials were placed in a cover-free sample-holder on a hot plate and heated at 60 °C for 5 h to completely evaporate the residual THF.

High-throughput screening workflow for photocatalytic hydrogen evolution

Vials (10.0 ml, Agilent Technologies) were charged with as-prepared photocatalyst solutions (5.0 ml) and transferred to a Chemspeed Accelerator SWING workstation. Degassed jars with stock solutions of H_2PtCl_6 and ascorbic acid were loaded into this automated liquid handling platform, which then dispensed aqueous H_2PtCl_6 solution (0.17 ml, 3 wt% Pt with respect to the photocatalysts) and ascorbic acid solution (0.20 ml, 1 M aqueous solution) followed by nitrogen purging for 4 h. The vials were capped automatically using the capper/crimper tool under inert conditions, and then removed and sonicated in an ultrasonic bath for 5 min. A solar simulator (AM 1.5G, class AAA, IEC/JIS/ASTM, 1,600 W xenon, 12 × 12 inches, model 94123A) was used to illuminate vials on a Stuart roller bar SRT9, and provided uniform irradiance for a maximum of 48 samples. After 2 h of photocatalysis, gaseous products were analysed on a Shimadzu GC-2010 (barrier discharge ionization detector, Rt-Msieve 5 Å column with helium as the carrier gas) equipped with a headspace injector (Shimadzu HS-20) in which a sample loop was used to enable continuous analysis via batch processing. No hydrogen evolution was observed for mixtures of water/ascorbic acid or water/ascorbic acid/H_2PtCl_6 under identical conditions. The hydrogen evolution measurements were repeated at least twice to confirm that the measurements were reproducible.

FNP for scaled-up production

Individual stock solutions (0.38 mg ml^{-1}) of donor molecules and acceptor molecules and were prepared in THF. Nanoparticle precursor solutions were prepared from the stock solutions by mixing them in the ratio of the desired nanoparticle composition. Then, 1 ml of surfactant S1 (0.50 mg ml^{-1} in THF) was added to the 10.0 ml nanoparticle precursor solution, which served as an organic stream (stream 1) for FNP. This organic stream was fed into a multi-inlet vortex mixer system with pure water streams (streams 2–4) at different fluxes (15 ml min^{-1} for streams 1 and 2, 30 ml min^{-1} for streams 3 and 4), using two digitally controlled syringe pumps (Harvard Apparatus, PHD 2000), to yield the colloidal solutions (at ~25 °C). The residual THF in the mixture was removed by heating at 35 °C in a water bath, finally affording a clear aqueous solution that contains nanojunction photocatalysts.

Photocatalytic hydrogen evolution measurement of FNP samples

Photocatalytic hydrogen evolution experiments for FNP samples were conducted in a glass gas-closed-circulation system (Labsolar-6A, Beijing Perfectlight). Typically, a quartz reactor was charged with colloidal solution (25.0 ml) containing 1.56 mg nanoparticles, ascorbic acid (0.2 M) and a certain amount of platinum as a co-catalyst using hexachloroplatinic acid as a platinum precursor. Before light irradiation, the dissolved air was thoroughly removed by a vacuum pump. The system was irradiated from the top using a 300 W xenon lamp (Perfectlight PLS-SXE300D). The temperature of the reaction solution was maintained at 10 °C by circulation of cool water. Because these nanoparticles were well dispersed, no stirring was needed during the photocatalytic reaction. The evolved gases were detected on an online gas chromatograph (Shimadzu GC 2014C) with a thermal conductivity detector.

EQE measurements

A 300 W xenon lamp with a monochromatic optical filter was used as the light source to perform the experiments to determine the apparent quantum yield, and a circular mask with an inner diameter of 30 mm was inserted to narrow the distribution of the light intensity. The EQEs were calculated using the following equation:

$$\mathrm{EQE}\,(\%) = \frac{2 \times \text{number of evolved } H_2 \text{ molecules}}{\text{number of incident photons}} \times 100\%$$

Data availability

Source data are provided with this paper. All other data supporting the findings of this study are available within this Article and its Supplementary Information. The X-ray crystallographic coordinates for structures reported in this study have been deposited at the Cambridge Crystallographic Data Centre (CCDC), under deposition numbers 2292568 and 2292583 for MTPA-CA and CNP147, respectively. These data can be obtained free of charge from CCDC via www.ccdc.cam.ac.uk/data_request/cif.

References

1. Yan, C. et al. Non-fullerene acceptors for organic solar cells. *Nat. Rev. Mater.* **3**, 18003 (2018).
2. Meng, L. et al. Organic and solution-processed tandem solar cells with 17.3% efficiency. *Science* **361**, 1094–1098 (2018).
3. Zhu, L. et al. Single-junction organic solar cells with over 19% efficiency enabled by a refined double-fibril network morphology. *Nat. Mater.* **21**, 656–663 (2022).
4. Abdurahman, A. et al. Understanding the luminescent nature of organic radicals for efficient doublet emitters and pure-red light-emitting diodes. *Nat. Mater.* **19**, 1224–1229 (2020).
5. Kabe, R. & Adachi, C. Organic long persistent luminescence. *Nature* **550**, 384–387 (2017).
6. Rivnay, J. et al. Organic electrochemical transistors. *Nat. Rev. Mater.* **3**, 17086 (2018).
7. Oh, J. Y. et al. Intrinsically stretchable and healable semiconducting polymer for organic transistors. *Nature* **539**, 411–415 (2016).
8. Wang, X. et al. A metal-free polymeric photocatalyst for hydrogen production from water under visible light. *Nat. Mater.* **8**, 76–80 (2009).
9. Zhang, W. et al. Reconstructed covalent organic frameworks. *Nature* **604**, 72–79 (2022).

10. Wang, Y. et al. Current understanding and challenges of solar-driven hydrogen generation using polymeric photocatalysts. *Nat. Energy* **4**, 746–760 (2019).
11. Wang, L. et al. Organic polymer dots as photocatalysts for visible light-driven hydrogen generation. *Angew. Chem. Int. Ed.* **55**, 12306–12310 (2016).
12. Wadsworth, A., Hamid, Z., Kosco, J., Gasparini, N. & McCulloch, I. The bulk heterojunction in organic photovoltaic, photodetector, and photocatalytic applications. *Adv. Mater.* **32**, 2001763 (2020).
13. Kosco, J. et al. Generation of long-lived charges in organic semiconductor heterojunction nanoparticles for efficient photocatalytic hydrogen evolution. *Nat. Energy* **7**, 340–351 (2022).
14. Wagen, C. C., McMinn, S. E., Kwan, E. E. & Jacobsen, E. N. Screening for generality in asymmetric catalysis. *Nature* **610**, 680–686 (2022).
15. Nieuwelink, A. et al. High-throughput activity screening and sorting of single catalyst particles with a droplet microreactor using dielectrophoresis. *Nat. Catal.* **4**, 1070–1079 (2021).
16. Allen, C. L., Leitch, D. C., Anson, M. S. & Zajac, M. A. The power and accessibility of high-throughput methods for catalysis research. *Nat. Catal.* **2**, 2–4 (2019).
17. Zhao, Y. et al. A bilayer conducting polymer structure for planar perovskite solar cells with over 1,400 hours operational stability at elevated temperatures. *Nat. Energy* **7**, 144–152 (2022).
18. Buitrago, S. A. et al. Nanomole-scale high-throughput chemistry for the synthesis of complex molecules. *Science* **347**, 49–53 (2015).
19. MacLeod, B. P. et al. Self-driving laboratory for accelerated discovery of thin-film materials. *Sci. Adv.* **6**, z8867 (2020).
20. Du, X. et al. Elucidating the full potential of OPV materials utilizing a high-throughput robot-based platform and machine learning. *Joule* **5**, 495–506 (2021).
21. Buglioni, L., Raymenants, F., Slattery, A., Zondag, S. D. A. & Noël, T. Technological innovations in photochemistry for organic synthesis: flow chemistry, high-throughput experimentation, scale-up, and photoelectrochemistry. *Chem. Rev.* **122**, 2752–2906 (2022).
22. Jäkel, C. & Paciello, R. High-throughput and parallel screening methods in asymmetric hydrogenation. *Chem. Rev.* **106**, 2912–2942 (2006).
23. Greenaway, R. L. et al. High-throughput discovery of organic cages and catenanes using computational screening fused with robotic synthesis. *Nat. Commun.* **9**, 2849 (2018).
24. Perera, D. et al. A platform for automated nanomole-scale reaction screening and micromole-scale synthesis in flow. *Science* **359**, 429–434 (2018).
25. Kosco, J. et al. Enhanced photocatalytic hydrogen evolution from organic semiconductor heterojunction nanoparticles. *Nat. Mater.* **19**, 559–565 (2020).
26. Yang, H., Li, X., Sprick, R. S. & Cooper, A. I. Conjugated polymer donor–molecular acceptor nanohybrids for photocatalytic hydrogen evolution. *Chem. Commun.* **56**, 6790–6793 (2020).
27. Liu, A. et al. Panchromatic ternary polymer dots involving sub-picosecond energy and charge transfer for efficient and stable photocatalytic hydrogen evolution. *J. Am. Chem. Soc.* **143**, 2875–2885 (2021).
28. Wang, S., Cai, B. & Tian, H. Efficient generation of hydrogen peroxide and formate by an organic polymer dots photocatalyst in alkaline conditions. *Angew. Chem. Int. Ed.* **61**, e202202733 (2022).
29. Zhu, Y. et al. Organic photovoltaic catalyst with extended exciton diffusion for high-performance solar hydrogen evolution. *J. Am. Chem. Soc.* **144**, 12747–12755 (2022).
30. Zhang, Z. et al. Two-dimensional polycyclic photovoltaic molecule with low trap density for high-performance photocatalytic hydrogen evolution. *Angew. Chem. Int. Ed.* **61**, e202114234 (2022).
31. Sun, Y. et al. Rational control of sequential morphology evolution and vertical distribution toward 17.18% efficiency all-small-molecule organic solar cells. *Joule* **6**, 2835–2848 (2022).
32. Zhang, Y. et al. H_2O_2 generation from O_2 and H_2O on a near-infrared absorbing porphyrin supramolecular photocatalyst. *Nat. Energy* **8**, 361–371 (2023).
33. Yang, H. et al. Packing-induced selectivity switching in molecular nanoparticle photocatalysts for hydrogen and hydrogen peroxide production. *Nat. Nanotechnol.* **18**, 307–315 (2023).
34. Pavliuk, M. V., Wrede, S. & Tian, H. Phenoxazine-based small molecule heterojunction nanoparticles for photocatalytic hydrogen production. *Chem. Commun.* **59**, 5611–5614 (2023).
35. Fuse, S. et al. Elucidation of the structure–property relationship of p-type organic semiconductors through rapid library construction via a one-pot, Suzuki–Miyaura coupling reaction. *ACS Comb. Sci.* **16**, 494–499 (2014).
36. Liu, L. et al. Linear conjugated polymers for solar-driven hydrogen peroxide production: the importance of catalyst stability. *J. Am. Chem. Soc.* **143**, 19287–19293 (2021).
37. Koumura, N. et al. Alkyl-functionalized organic dyes for efficient molecular photovoltaics. *J. Am. Chem. Soc.* **128**, 14256–14257 (2006).
38. Zhang, W. et al. Molecular engineering and sequential cosensitization for preventing the 'trade-off' effect with photovoltaic enhancement. *Chem. Sci.* **8**, 2115–2124 (2017).
39. Yu, M., Zhang, W., Guo, Z., Wu, Y. & Zhu, W. Engineering nanoparticulate organic photocatalysts via a scalable flash nanoprecipitation process for efficient hydrogen production. *Angew. Chem. Int. Ed.* **60**, 15590–15597 (2021).
40. Liu, A. et al. Excited-state and charge-carrier dynamics in binary conjugated polymer dots towards efficient photocatalytic hydrogen evolution. *Phys. Chem. Chem. Phys.* **25**, 2935–2945 (2023).
41. Zhang, Y. et al. Tailored energy funneling in photocatalytic π-conjugated polymer nanofibres for high-performance hydrogen production. *J. Am. Chem. Soc.* **145**, 22539–22547 (2023).
42. Bannwarth, C., Ehlert, S. & Grimme, S. GFN2-xTB—an accurate and broadly parametrized self-consistent tight-binding quantum chemical method with multipole electrostatics and density-dependent dispersion contributions. *J. Chem. Theory Comput.* **15**, 1652–1671 (2019).
43. Grimme, S., Bannwarth, C. & Shushkov, P. A robust and accurate tight-binding quantum chemical method for structures, vibrational frequencies, and noncovalent interactions of large molecular systems parametrized for all *spd*-block elements (Z=1–86). *J. Chem. Theory Comput.* **13**, 1989–2009 (2017).
44. Yanai, T., Tew, D. P. & Handy, N. C. A new hybrid exchange–correlation functional using the Coulomb-attenuating method (CAM-B3LYP). *Chem. Phys. Lett.* **393**, 51–57 (2004).
45. Weigend, F. & Ahlrichs, R. Balanced basis sets of split valence, triple zeta valence and quadruple zeta valence quality for H to Rn: design and assessment of accuracy. *Phys. Chem. Chem. Phys.* **7**, 3297–3305 (2005).
46. Weigend, F. Accurate Coulomb-fitting basis sets for H to Rn. *Phys. Chem. Chem. Phys.* **8**, 1057–1065 (2006).
47. Frisch, M. J. et al. Gaussian 16, rev. C.01 (2016).
48. Brown, J. S. CATNIP, v.1.9 (2019); https://github.com/JoshuaSBrown/QC_Tools
49. Liu, T. & Troisi, A. Absolute rate of charge separation and recombination in a molecular model of the P3HT/PCBM interface. *J. Phys. Chem. C.* **115**, 2406–2415 (2011).

50. Mclnnes, L., Healy, J. & Melville, J. UMAP: uniform manifold approximation and projection for dimension reduction. Available at: https://arxiv.org/abs/1802.03426 (2018).

Acknowledgements

We thank the National Natural Science Foundation of China (NSFC, 22338006, 22372151, 9235630033 and 22375062); Shanghai Municipal Science and Technology Major Project (2018SHZDZX03, 21JC1401700); the Shanghai Pilot Program for Basic Research (22TQ1400100-10); Shanghai Municipal Science and Technology (20120710200); Fundamental Research Funds for the Central Universities; the Shanghai Pujiang Program (22PJ1402400); the 'Chenguang Program' supported by the Shanghai Education Development Foundation and the Shanghai Municipal Education Commission (22CGA32); the Engineering and Physical Sciences Research Council (EPSRC) for financial support under grants EP/N004884/1 and EP/P034497/1; and the Leading Innovative and Entrepreneur Team Introduction Program of Zhejiang (2022R01007). W.Z. acknowledges the Young Elite Scientists Sponsorship Program by CAST (2023QNRC001) and the Research Center of Analysis and Test of East China University of Science and Technology (ECUST) for assistance with various characterizations and C. Zhao from ECUST for useful discussion on theoretical calculations. M.Y. acknowledges the China Scholarship Council (CSC) for financial support. A.I.C. thanks the Royal Society for a Research Professorship (RSRP\S2\232003).

Author contributions

W.Z., X. Li, W.-H.Z. and A.I.C. conceived the project. X. Li designed and synthesized CNPs and conducted high-throughput screening. W.Z., S.Z. and H.G. synthesized and characterized other molecules. M.Y., X. Liu and Y.B. performed the photocatalysis experiments. X. Liu performed the electron microscopy characterizations. T.L. performed the simulations. M.C. and Z.Z. conducted the transient absorption spectroscopy. M.Y., H.Y. and Y.W. carried out the optical spectra measurements. Q.Z. performed the single-crystal X-ray diffraction measurements. W.Z., X.W., H.T., X.Li, W.-H.Z. and A.I.C. analysed the data and wrote the paper. All authors discussed the results and commented on the manuscript.

Competing interests

The authors declare no competing interests.

Additional information

Supplementary information The online version contains supplementary material available at https://doi.org/10.1038/s44160-024-00494-9.

Correspondence and requests for materials should be addressed to Xiaobo Li, Wei-Hong Zhu or Andrew I. Cooper.

Peer review information *Nature Synthesis* thanks Charles Schroeder, Haining Tian and the other, anonymous, reviewer(s) for their contribution to the peer review of this work. Primary Handling Editor: Alison Stoddart, in collaboration with the *Nature Synthesis* team.